Title

Magnetic Materials: Experimental Evidence of Chiral Ferrimagnetism in Amorphous GdCo Films (Adv. Mater. 27/2018)

Journal

Advanced Materials, 30(27)

ISSN

0935-9648

Authors

Streubel, Robert
Lambert, Charles-Henri
Kent, Noah
et al.

Publication Date

2018-07-01

DOI

10.1002/adma.201870200

Peer reviewed

ADVANCED MATERIALS
www.advmat.de

Experimental Evidence of Chiral Ferrimagnetism in Amorphous GdCo Films

Robert Streubel, Charles-Henri Lambert, Noah Kent, Peter Ercius, Alpha T. N'Diaye, Colin Ophus, Sayeef Salahuddin, and Peter Fischer*

Inversion symmetry breaking has become a vital research area in modern magnetism with phenomena including the Rashba effect, spin Hall effect, and the Dzyaloshinskii–Moriya interaction (DMI)—a vector spin exchange. The latter one may stabilize chiral spin textures with topologically nontrivial properties, such as Skyrmions. So far, chiral spin textures have mainly been studied in helimagnets and thin ferromagnets with heavy-element capping. Here, the concept of chirality driven by interfacial DMI is generalized to complex multicomponent systems and demonstrated on the example of chiral ferrimagnetism in amorphous GdCo films. Utilizing Lorentz microscopy and X-ray magnetic circular dichroism spectroscopy, and tailoring thickness, capping, and rare-earth composition, reveal that 2 nm thick GdCo films preserve ferrimagnetism and stabilize chiral domain walls. The type of chiral domain walls depends on the rare-earth composition/saturation magnetization, enabling a possible temperature control of the intrinsic properties of ferrimagnetic domain walls.

The emergence of an ordered magnetization configuration with a (local) magnetic moment primarily originates from spin exchange and spin–orbit interactions leading, with few exceptions, to the well-known parallel and antiparallel alignment of neighboring spins in ferromagnetic, ferrimagnetic and antiferromagnetic materials. Exceptions include inversion symmetry breaking systems which possess a vector spin exchange known as Dzyaloshinskii–Moriya interaction (DMI),[1,2] in addition to the scalar Heisenberg exchange term. Recent research has demonstrated that surfaces and interfaces can break inversion symmetry and induce a considerable interfacial DMI[3,4] and an associated chirality selection.[5–9] In fact, it is the spin texture at interfaces, that has become subject to intense research in view of both fascinating fundamental physics and novel approaches to spin based technologies[10] due to emergent phenomena such as spin Hall effect,[11] interfacial DMI, and capability to design composite heterostructural materials with unique properties scarcely accessible in bulk materials. While ferromagnets have extensively been used for those investigations, the growing interest in ferrimagnetic and antiferromagnetic materials takes advantage of (nearly) compensated spins and the associated insensitivity against external magnetic fields. Moreover, ferrimagnets can bridge the gap between ferromagnetism and antiferromagnetism, which is a fundamentally interesting endeavor in view of spin orbitronics,[12] spin caloritronics,[13,14] all-optical switching,[15,16] and phase transitions.[17] Ferrimagnets are superior to theoretically proposed chiral antiferromagnets[18] since they do not require epitaxial growth. In fact, ferrimagnets composed of rare-earth elements and transition metals form amorphous composites and distinctly interact with magnetic exchange,[19] and potentially with spin current and magnons. Both aspects are essential for future applications, to provide precise addressability and to avoid spin frustration and magnetic pinning. In this respect, chiral ferrimagnetic metals are distinct and superior to chiral molecules, which possess chiral ferrimagnetism near absolute zero.[20] Aside from prospective applications as magnetic racetrack/logic devices[21,22] based on ferrimagnetic Skyrmions/chiral bubbles, chiral ferrimagnetism in inorganic materials allows all-optical switching of chiral spin textures,[23] studying spin fluctuations of topological phases and phase transitions,[17] and generalizing the concept of chirality driven by interfacial DMI to more complex multicomponent systems.

Whereas thick (>20 nm) ferrimagnetic films with bulk-like properties are well understood[16,24–28] owing to prospective applications in heat assisted magnetic recording[29] or all-optical

Dr. R. Streubel, N. Kent, Dr. P. Fischer
Materials Sciences Division
Lawrence Berkeley National Laboratory
Berkeley, CA 94720, USA
E-mail: streubel@lbl.gov
Dr. C.-H. Lambert, Prof. S. Salahuddin
Department of Engineering
University of California
Berkeley, CA 94720, USA
N. Kent, Dr. P. Fischer
Physics Department
UC Santa Cruz
Santa Cruz, CA 95064, USA
Dr. P. Ercius, Dr. C. Ophus
Molecular Foundry
Lawrence Berkeley National Laboratory
Berkeley, CA 94720, USA
Dr. A. T. N'Diaye
Advanced Light Source
Lawrence Berkeley National Laboratory
Berkeley, CA 94720, USA

DOI: 10.1002/adma.201800199

switching,[15,16] information about thin (<5 nm) ferrimagnetic layers are rare in literature and has just recently attracted attention.[30–32] Ferrimagnetism in amorphous rare-earth materials originates from distinct electron configurations (Hund's rules) in early rare-earth elements (Tb, Gd) and transition metals (Fe, Co, Ni) that favor an antiparallel alignment due to negative indirect exchange coupling.[19] Same elements (Tb or Gd atoms) align ferromagnetically. A preferential magnetization orientation is manifested by a chemical anisotropy in short-range order of atoms due to different distances and elements. Such an anisotropy can naturally be induced by cosputtering or subsequent sputtering rare-earth elements and transition metals leading to a perpendicular magnetic anisotropy as shown for TbFe.[26–28] The individual contributions of the ferromagnetic and ferrimagnetic subsystems are temperature and composition dependent.

Here, we report experimental evidence of chiral ferrimagnetism in amorphous GdCo multilayer stacks with perpendicular magnetic anisotropy sandwiched between heavy-element metals by means of quantitative X-ray magnetic circular dichroism (XMCD) spectroscopy and high-resolution Lorentz microscopy with exit wave reconstruction. Our results show that the analysis of magnetic domain morphology and magnetization reversal process alone is insufficient to judge the nature of the domain walls and their chirality. Tailoring thickness, capping, and rare-earth composition, we find that a 2 nm thick GdCo film preserves ferrimagnetism with a substantial rare-earth contribution while stabilizing chiral domain walls through a significant interfacial Dzyaloshinskii–Moriya interaction. The type of chiral domain walls (Néel, hybrid Néel-Bloch walls) depends on the rare-earth composition of the ferrimagnet. Lower thicknesses cause a quenching of the net Gd spin moment originating from an insufficient indirect Gd–Co exchange interaction.[19] The thickness independent Co spin moment strongly experiences varying heavy-element capping. Experimentally, the low saturation magnetization of the samples requires a novel approach to retrieve the magnetic induction from the microscopic Lorentz data, that is superior in terms of spatial and contrast resolution to the commonly used transport-of-intensity equation,[33,34] but less demanding than magnetic tomography techniques.[35–38]

We prepared ferrimagnetic multilayer stacks that were deposited at room temperature by dc magnetron cosputtering of pure Gd and Co targets at rates of (0.1–0.5) A s^{-1} (base pressure: 5×10^{-8} Torr; Argon pressure: 3.5 mTorr) on various Si and SiN substrates. To improve uniformity of the films, the substrate was rotating at (30–50) rpm. Films were simultaneously deposited onto thermally oxidized Si wafers, and SiN nanomembranes with a window thickness of 30 nm (Lorentz microscopy) and 100 nm (X-ray microscopy). The growth conditions were optimized to minimize film roughness (RMS <0.1 nm) and structural inhomogeneities, both essential for (ultra) thin multilayer stacks and Lorentz microscopy. The rare-earth composition of each sample was determined utilizing Rutherford backscattering and X-ray absorption spectroscopy with an uncertainty of about 2%. X-ray absorption spectroscopy also confirmed metallic Co and Gd.

To understand the dependence of ferrimagnetism in amorphous thin films, including, e.g., spin compensation, saturation magnetization, coercive fields, and anisotropy, on the film thickness, we prepared ferrimagnetic GdCo multilayer stacks with a GdCo thickness ranging from 1 to 5 nm (**Table 1**). Additionally, a 15 nm thick GdCo layer sample was used as reference with bulk-like properties. Each GdCo layer is sandwiched between heavy-element materials (Ir or Pt) to obtain a large interfacial DMI at the GdCo interface acting on the Co spins.[39] Samples with symmetric (Pt, Pt) and asymmetric (Pt, Ir) stacking are labeled as SX and AX, respectively, where X denotes the GdCo layer thickness in nanometer. The vertical spacing between the GdCo layers is set to 2 nm (or 4 nm for A1 and S1) for both symmetric and asymmetric stack to guarantee the most similar properties and to prevent any unintended negative interlayer exchange causing antiparallel alignment of adjacent layers. Among all theoretically studied heavy-element materials, Ir and Pt provide the largest interfacial DMI on Co spins with opposite signs,[39] allowing for the largest possible (asymmetric) or nearly vanishing (symmetric) net DMI value. As evident from our work, the results calculated with spin density functional theory (DFT) for epitaxial ferromagnetic Co[39] allow also for drawing qualitative conclusions on, e.g., sign and strength of DMI in amorphous ferrimagnetic GdCo systems. We chose rare-earth compositions in the range x = (18–24)% (Co dominated) to stabilize out-of-plane magnetized multidomain states and magnetic domain walls at room temperature and at remanence. Note that thick ferrimagnets with such a composition possess a very low room temperature saturation magnetization of about 150 kA m^{-1} and do not split up into domains.

The GdCo multilayer stacks were screened by recording both out-of-plane and in-plane magnetic hysteresis loops, and determining saturation magnetization and perpendicular magnetic anisotropy. The magnetization reversal processes were

Table 1. Investigated ferrimagnetic multilayer stacks. One repetition consists of bottom, ferrimagnetic and top layers. The notation is chosen for simplicity with S and A referring to symmetric and asymmetric stacks, respectively, followed by an integer indicating the GdCo thickness of a single layer. The index highlights the rare-earth atomic composition; A missing index implies $x = (21 \pm 2)$%.

Notation	Bottom	Ferrimagnet	Top	Repetition
Rare-earth composition $x = (21 \pm 2)$%				
S1	Pt(2 nm)	$Gd_{21}Co_{79}$(1 nm)	Pt(2 nm)	50
S2	Pt(1 nm)	$Gd_{21}Co_{79}$(2 nm)	Pt(1 nm)	15
A1	Ir(2 nm)	$Gd_{21}Co_{79}$(1 nm)	Pt(2 nm)	50
A2	Ir(1 nm)	$Gd_{21}Co_{79}$(2 nm)	Pt(1 nm)	15
A3	Ir(1 nm)	$Gd_{21}Co_{79}$(3 nm)	Pt(1 nm)	12
A4	Ir(1 nm)	$Gd_{21}Co_{79}$(4 nm)	Pt(1 nm)	10
A5	Ir(1 nm)	$Gd_{21}Co_{79}$(5 nm)	Pt(1 nm)	8
Rare-earth composition $x = (18 \pm 2)$%				
$A2_{18}$	Ir(1 nm)	$Gd_{18}Co_{82}$(2 nm)	Pt(1 nm)	15
...				
Rare-earth composition $x = (24 \pm 2)$%				
$A2_{24}$	Ir(1 nm)	$Gd_{24}Co_{76}$(2 nm)	Pt(1 nm)	15
$A15_{24}$	Ir(1 nm)	$Gd_{24}Co_{76}$(15 nm)	Pt(1 nm)	2
...				

investigated on the macro and microscale using vibrating sample magnetometry (VSM) and transmission X-ray microscopy (TXM), respectively. The latter used XMCD as magnetic contrast and was performed at beamline 6.1.2 at the Advanced Light Source (Berkeley, CA). Samples with very thin GdCo layers, i.e., 1 and 2 nm, do not reveal an obvious relation between hysteresis loops and GdCo film thickness or capping (**Figure 1**a), which is also reflected by the domain morphology and their evolution with out-of-plane magnetic field (Figure 1c). In fact, GdCo samples S1 and A1 reveal a domain morphology characteristic to ferromagnetic films without and with large DMI, and corresponding achiral Bloch and chiral Néel walls, respectively. Contrarily, the 2 nm thick samples S2 and A2 show similar domain patterns but different feature sizes due to distinct saturation magnetizations (Figure 1b) and weaker DMI. A closer look at the magnetic domains of S2 and A2 unveils areas (indicated by white arrows) where the XMCD contrast at the Co L_3 edge is inverted compared to the surrounding domain and unaffected by the magnetic field, respectively. This is because of segregation and local variation of the rare-earth composition leading to either a net magnetization governed by the enlarged Gd moment and an antiparallel alignment of the Co magnetization with respect to the surrounding domain, or a significantly increased switching field.

Analyzing the saturation magnetization and the in-plane magnetic hysteresis loops (Figure 1b) provided further details on the magnetic properties including domain morphology: firstly, a linear decrease in the saturation magnetization with increasing GdCo thickness for $t \leq 4$ nm (slope: $-(50 \pm 2)$ kA m^{-1} nm^{-1}); secondly, an increased saturation magnetization of the symmetric samples with respect to the asymmetric ones by a factor of $c_{SA} = 1.3 \pm 0.1$, i.e., $c_{SA}(1) = \frac{M_s(S_1)}{M_s(A_1)} = 1.3 \pm 0.1$; $c_{SA}(2) = \frac{M_s(S_2)}{M_s(A_2)} = 1.3 \pm 0.1$; and, thirdly, a decrease in the magnitude of the perpendicular magnetic anisotropy with increasing GdCo thickness toward the bulk value of ≈10 kJ m^{-3}. These modifications originate from both enlarged surface-to-volume ratio and spin–orbit coupling at the interfaces. The alignment of the Gd magnetization in the amorphous compound relies on the negative indirect exchange interaction with Co:[19] the thinner the film, the less efficient the structurally induced magnetic anisotropy. Simultaneously, Co experiences a large

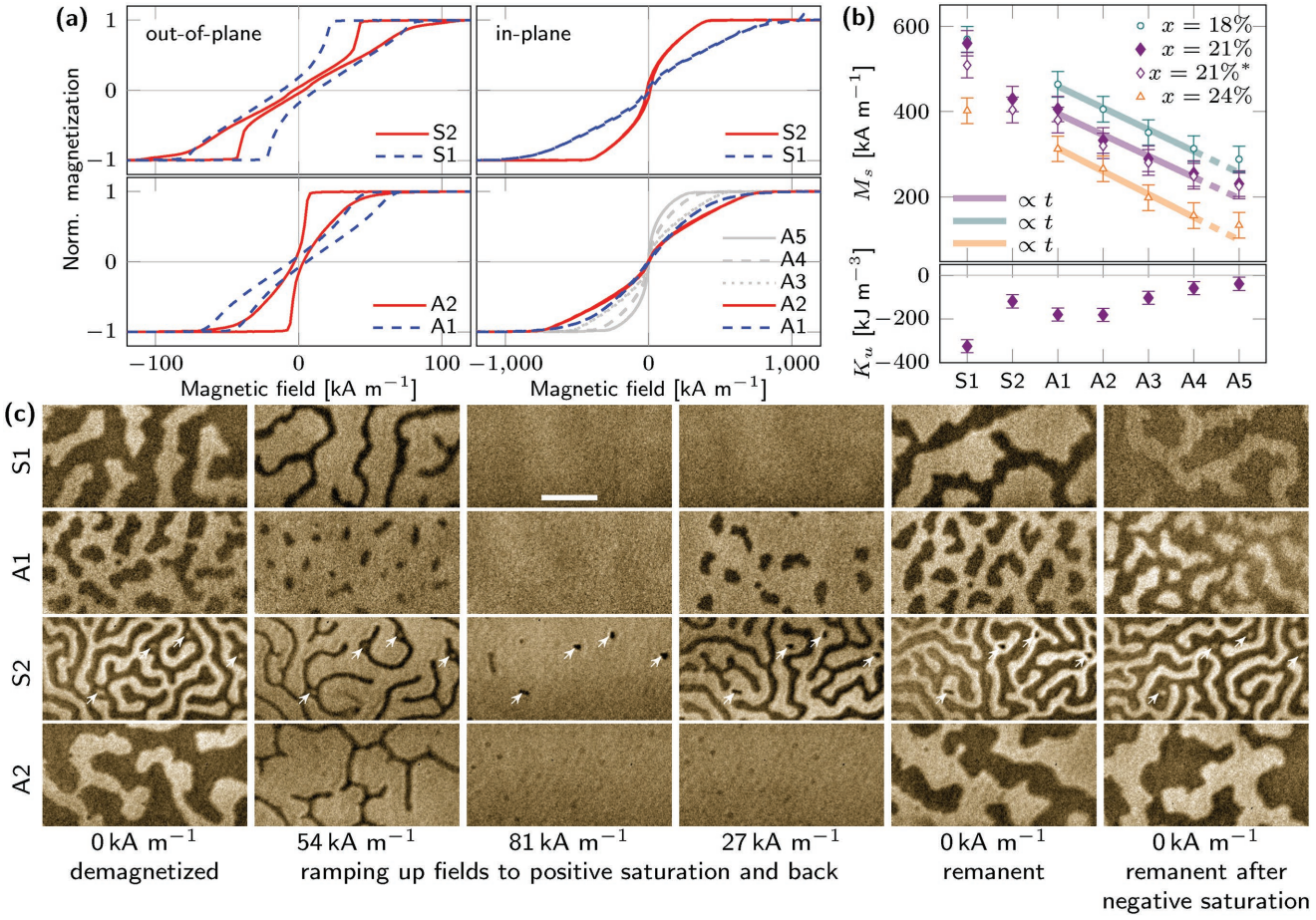

Figure 1. Magnetization reversal processes in symmetric and asymmetric ferrimagnetic GdCo multilayer stacks with perpendicular magnetic anisotropy. a) Magnetic hysteresis loops recorded at room temperature with VSM. b) Saturation magnetization M_s and perpendicular magnetic anisotropy K_u for various GdCo thicknesses and rare-earth composition $x = (18 \pm 2)\%$, $x = (21 \pm 2)\%$, $x = (24 \pm 2)\%$. Curve 21%* shows the saturation magnetization with a deducted proximity Pt magnetization of 0.3 μ_B at the interfaces to GdCo. c) Selected images of the magnetization reversal process spatially resolved with TXM and XMCD at Co L_3 edge. The white arrows indicate local segregation of Gd-rich regions. Scale bar is 1 µm; Field of view is the same for each image.

magnetic anisotropy at the interface to Pt and Ir causing a substantial net Co moment and an enhanced perpendicular magnetic anisotropy of the Gd–Co spin system. Indeed, rare-earth compositions close to 20% manifest a perpendicular magnetic anisotropy in thin films that turns in-plane in thick films (≥15 nm) with a significantly reduced net magnetization (150 kA m^{-1}). The enlarged saturation magnetization in thin ferrimagnetic films (≤4 nm) can be compensated by increasing the rare-earth composition by ≈10% with respect to bulk systems or by ≈3% per reduced nanometer of the GdCo layer thickness (Figure 1b). The prominent difference of the saturation magnetization for symmetric and asymmetric stacks can only be explained by the impact of Ir or Pt. Considering a typical proximity Pt magnetization of 0.3 μ_B induced by the Co magnetization at the interfaces[39,40] does not sufficiently enlarge the saturation magnetization to resolve this discrepancy (Figure 1b). This leaves three possible mechanisms: i) the Pt (Ir) capping disfavors (improves) the alignment of Gd spins; ii) the growth on Ir is worse than on Pt, which leads to rough interfaces and hence worse alignment of the Co spins; or iii) the induced proximity Pt magnetization is larger than that predicted for epitaxial layers due to intermixed amorphous interfaces. As we show below, the second mechanism is the leading contribution. For the 2 nm thick samples, a similar saturation magnetization for symmetric and asymmetric GdCo stacks can be obtained using 21% (S2) and 18% ($A2_{18}$), respectively.

In order to understand the individual contributions and to verify ferrimagnetism in our samples, we performed XMCD spectroscopy, and quantified the spin and orbital moments of Gd and Co via the well-known XMCD sum rules.[41,42] XMCD spectroscopy was performed at beamline 6.3.1 at the Advanced Light Source (Berkeley, CA). The X-ray absorption spectra (XAS) near the Co $L_{3,2}$ [(750–850) eV] and the Gd $M_{5,4}$ [(1150–1255) eV] edges were recorded while applying an external magnetic field (±200 kA m^{-1}) normal to the sample surface. Monitoring the current of electrons emanating from the surface provides a probing depth of about 6 nm and hence allows to retrieve information from the magnetization in the first one or two GdCo layers. We calculated the integrals

$$\left.\begin{aligned} r &= \int_{L_3+L_2} (\mu_+ + \mu_-)\mathrm{d}\omega \\ q &= \int_{L_3+L_2} (\mu_+ - \mu_-)\mathrm{d}\omega \\ p &= \int_{L_3} (\mu_+ - \mu_-)\mathrm{d}\omega \end{aligned}\right\} \quad (1)$$

and quantified the orbital (m_o) and spin (m_s) moment according to[41,42]

$$\left.\begin{aligned} m_o &= -\frac{4q}{3r} n_h \\ m_s &= -\frac{6p-4q}{r} n_h \left(1 + \frac{7\langle T_z\rangle}{2\langle S_z\rangle}\right)^{-1} \end{aligned}\right\} \quad (2)$$

An electron hole density of 2.5 (Co) and 7 (Gd) was used. Note that the expectation value of the magnetic dipole operator $\langle T_z\rangle$ is negligible in systems without large anisotropy and usually neglected in transition metals (Co: $\langle T_z\rangle/\langle S_z\rangle \approx -0.26\%$).[43] At the surface, it may increase up to 16 times[43] causing an actual m_s that is 117% of the determined (bulk) value. However, interfaces with an engineered large asymmetry/anisotropy as induced by heavy-element capping layers will substantially increase contributions by the magnetic dipole operator $\langle T_z\rangle$.

Figure 2a plots examples of X-ray absorption spectra (XAS) and XMCD signal near the Co $L_{3,2}$ and the Gd $M_{5,4}$ edges for asymmetric GdCo (A2) saturated out-of-plane in an external magnetic field (±200 kA m^{-1}). The XMCD signals prove the ferrimagnetism with Co spins aligned at room temperature along the magnetic field direction for any thickness and rare-earth composition x = (18–24)%. More quantitatively, the data show that the Co magnetization is within errors unaffected by either thickness or composition, and is slightly smaller than bulk values (m_s^{Co} = 1.6 μ_B per atom; m_o^{Co} = 0.15 μ_B per atom[44]) (Figure 2b,c). The smaller saturation magnetization is in parts caused by the amorphous film morphology leading to less

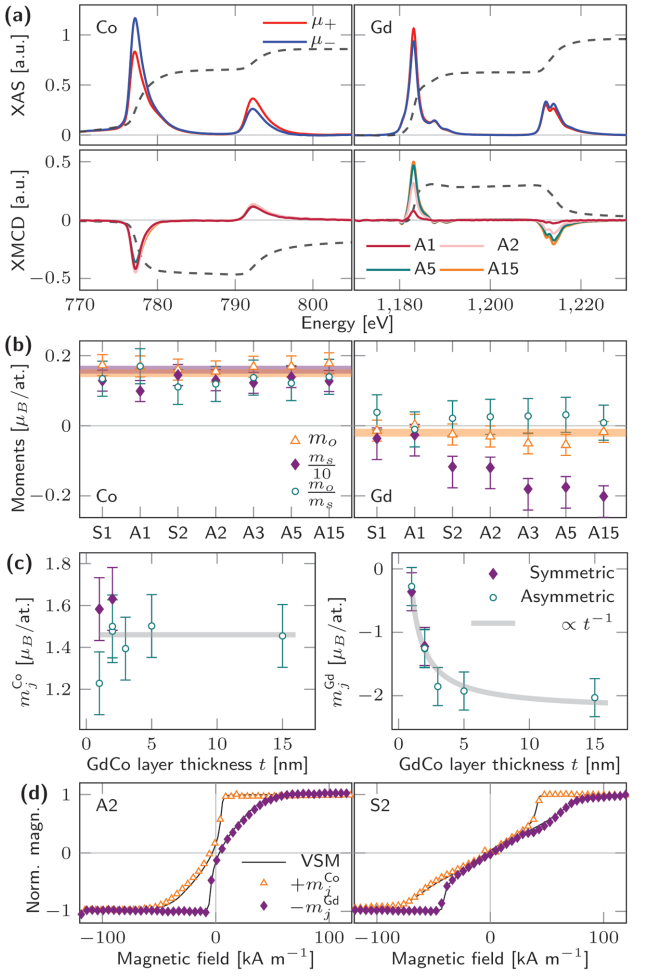

Figure 2. Quantification of ferrimagnetism using XMCD spectroscopy. a) X-ray absorption spectra near Co $L_{3,2}$ and Gd $M_{5,4}$ edges shown for asymmetric GdCo (A2) saturated out-of-plane in ± 200 kA m^{-1}. Dashed lines plot the integrals used for quantitative analysis as defined in the text. b) Spin and orbital moments as well as their ratio for various symmetric and asymmetric samples. Colored horizontal lines indicate bulk values from literature. c) Thickness dependence of Co and Gd magnetization. d) Element-specific out-of-plane magnetic hysteresis loops revealing antiparallel coupling of normal magnetization components. Half of each loop is plotted for visibility.

ordered atoms and spins. Particularly, the Co spin moment of very thin GdCo films exhibit a significant dependence on the capping layer. The ratio between the saturation magnetization of symmetric and asymmetric stack, c_{SA} declared above, takes $c_{SA}(1) = 1.3 \pm 0.1$ and $c_{SA}(2) = 1.1 \pm 0.1$ (Figure 2c), which is in excellent agreement with $c_{SA} = 1.3 \pm 0.1$ derived from VSM. Consequently, the difference in saturation magnetization of symmetric and asymmetric stack originates largely from varying growth conditions of Co on Pt and Ir.

In contrast, the net Gd spin moment is quenched for thin films and significantly deviates from its bulk value ($m_s^{Gd} = -0.02\ \mu_B$ per atom; $m_o^{Gd} = -7.0\ \mu_B$ per atom at 0 K[45]) for thicknesses ≤2 nm (Figure 2b). It is independent of rare-earth composition and capping; the orbital moment remains zero within experimental uncertainty. Plotting the Gd spin moment as a function of the GdCo layer thickness unveils a t^{-1} relation suggesting an interface effect (Figure 2c). The origin of the interface contributions is twofold. Highly asymmetric interfaces with large spin–orbit coupling demand a modification of the spin moment sum rule[41,42] considering the typically negligible magnetic dipole operator. This adjustment addresses the mixing of $3d_{5/2}$ and $3d_{3/2}$ components due to 3d–4f exchange interaction which leads to spin-flip and orbital-flip processes that lower the measured $M_{5,4}$ absorption.[45] Although, it is negligible for bulk Gd with its isotropic s shells ($\langle T_z\rangle/\langle S_z\rangle \approx -0.29\%$),[45] modifications due to interface symmetry breaking are expected to be even more considerable than for transition metals. In this respect, the calculated spin moments represent a lower boundary. Although its actual contribution to the spin moment is unclear, it is reasonable to expect a factor of 1–2 at the interface.[43,45] Hence, the governing mechanism is the ordering of the Gd spins that improves in thicker films. For layer thicknesses ≤3 nm, the Gd spin moment can be described by a linear function of the thickness (analogously to Figure 1b, since Co magnetization thickness independent), which is consistent with the physical origin of the Gd spin ordering, namely the increase of the structurally induced magnetic anisotropy that eventually saturates in thick films ($t > 5$ nm), resembling a t^{-1} dependence (Figure 2c).

In spite of these distinct characteristics, the Co and Gd spins are strongly correlated, i.e., their normal magnetizations are antiparallel, via indirect exchange as proven by element resolved magnetization reversal processes. Figure 2d plots exemplarily the magnetic hysteresis loops of S2 and A2. Note that merely half of either Gd or Co loops are shown for better visibility and direct comparison to the VSM data, accounting for absent exchange bias.

In order to judge the chiral nature of the present ferrimagnets, we visualized the ferrimagnetic domain walls utilizing Lorentz microscopy. Here, we focus on 2 nm thick GdCo films since thinner systems lack ferrimagnetism (Figure 2b,c) and thicker ones stabilize achiral Bloch walls. Probing the magnetic induction perpendicularly to the propagation direction provides a sensitivity only to the in-plane components originating from magnetic domain walls that allows for unambiguously identifying domain wall type and chirality. Visualization of the ferrimagnetic domain walls was carried out using the aberration corrected transmission electron microscope (TEAM1) at the National Center for Electron Microscopy (Berkeley, CA). Operating in Lorentz mode at remanence and room temperature, we recorded the electron intensity with a direct electron detector (pixel size at 2000 ×: ≈ 0.45 nm) at 300 keV and various focal planes $\Delta f_k = (0\text{–}{-}5)$ mm whose change is associated with a phase accumulation due to interaction with the electromagnetic fields. The defoci were directly calculated from the power spectral density analyzing the minima according to

$$\Delta f_k = -n_k/\left(\lambda q_{0,k}^2\right) \tag{3}$$

with the $n_{k\text{-th}}$ minima located at $q_{0,k}$ and electron wavelength λ. For large defoci, the uncertainty originating from very few, small Thon rings becomes substantial (tens of percent), which affects the reconstruction. This limitation is overcome by back propagation of the focal planes into focus, which simultaneously improves alignment to ≈10 nm. Note that for large defocus values, alignment of the image series includes translation, rotation (up to 5°), scaling (up to 20%) operations.

The magnetic contribution to the electron phase shift ϕ originates from the Lorentz force acting on the propagating electrons and can be written in reciprocal space as

$$\phi_m\left(q_x, q_y\right) = \frac{i\pi\mu_0 M_s t N}{\Phi_0} \times \frac{m_x q_y - m_y q_x}{q_x^2 + q_y^2} \tag{4}$$

with the magnetic flux quantum Φ_0, unit magnetization vector component $m_{x,y}$, and reciprocal unit vector component $q_{x,y}$. M_s, t, and N are saturation magnetization, GdCo film thickness, and number of repetitions, respectively. The formula assumes a homogeneous magnetic configuration along the electron trajectory normal to the surface (z axis), which is in our thin samples a justified approximation. Whereas the phase information is usually lost in microscopy, Lorentz microscopy exploits the propagation of an initially planar electron wave front ψ_0 as $\Gamma_f\ \psi_0\ e^{i\phi}$ with the propagator Γ_f and the phase information $e^{i\phi}$. Information on the phase can be obtained from the intensity change taking advantage of the relationship between forward and backward (Γ_b) propagation

$$\Gamma_{(f,b)} = \exp[\pm(i\pi q^2 \Delta f_k + \chi)] \tag{5}$$

For magnetic Lorentz microscopy with a spatial resolution of ≈10 nm at 2000× magnification, the aberrations χ may be neglected in first approximation. We perform an iterative exit wave reconstruction applying the Gerchberg-Saxton (GS) reconstruction algorithm[46] to self-consistently retrieve both electron phase and in-plane magnetic induction. A quantitative analysis of electron phase/magnetic induction as a function of projection/tilt angle is used to identify both type and chirality of the ferrimagnetic domain wall.

Figure 3 depicts examples for symmetric and asymmetric GdCo films that were reconstructed from the electron intensities recorded at ≈20 focal planes ranging from 0 up to −5 mm, which is 100× larger than typical values. The focal series of both experimental and reconstructed electron intensities are shown in Movies S1–S8 (Supporting Information). The intensity variation originating from the interaction with the in plane magnetic induction becomes visible only at a defocus ≥1 mm. The spatial resolution of the reconstruction is limited by pixel size and alignment of the data to ≈10 nm

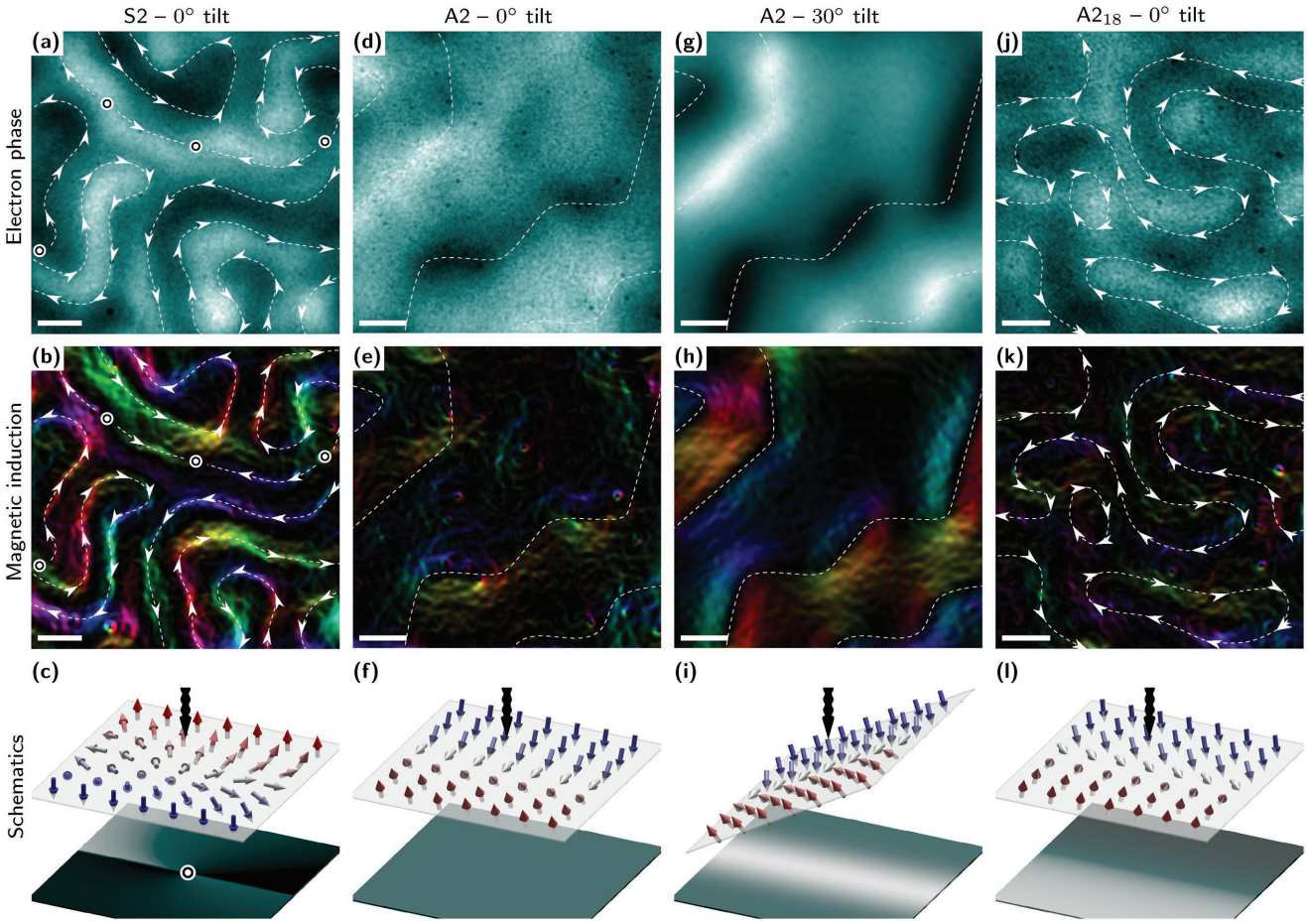

Figure 3. Domain wall imaging in symmetric and asymmetric GdCo facilitating Lorentz microscopy with exit wave reconstruction. a,d,g,j) Electron phase and b,e,h,k) magnetic induction retrieved from electron intensities at ≈20 focal planes, i.e. (0—5) mm. The dashed lines indicate domain walls with the arrows highlighting the chirality of Bloch and hybrid Bloch-Néel walls. The white-black circles mark the position of Bloch lines. Scale bars are 200 nm. Electron phase and magnetic induction are clipped to the strongest contrast, which is in all cases but (g,h) equal to structural defects (quasi normalized). c,f,i,l) Schematics and simulated phase of a Bloch line, Néel wall at normal and oblique incidence, and hybrid Bloch-Néel wall, respectively.

(at 2000× magnification) as evident from structural defects in the reconstructed electron phase (dark dots). At this magnification, intrinsic properties of the electron microscope/electron beam play a minor role when well aligned. In general, regions with homogeneous phase contrast refer to magnetic domains with an out-of-plane magnetization (compare with Figure 1c). The in-plane magnetic induction of the magnetic domain walls is obtained as the 2D spatial derivative of the phase, according to Equation (4).

The symmetric (S2) GdCo film exhibits Bloch walls whose magnetization orientation is indicated by arrows decorated on dashed white lines in Figure 3a,b. Since the system consists of Pt bottom and top layers with (virtually) compensating interfacial DMI, both domain wall chiralities are equally favorable. A chirality change is accompanied by the formation of two Bloch lines (Figure 3c) with an additional energy. The visualization of magnetic defects, such as Bloch points and Bloch lines, is highly interesting not only with respect to fundamental sciences, but also for storage and logic applications due to their high stability, similar to Skyrmions. It is however experimentally challenging, due to structural confinement and nearly compensating spins. Nevertheless, the stray field of those spin textures has been visualized with Lorentz microscopy (white-black markers in Figure 3a,b). The existence of Bloch lines is equal to a chirality change and is taken as an indicator of the same when studying Néel domain walls that are invisible in Lorentz microscopy.

Asymmetric GdCo (A2) films with an emergent interfacial DMI reveal an essentially different phase contrast/magnetic induction (Figure 3d,e,g,h). The nearly vanishing contrast for normal incidence (Figure 3d–f) is due to electron deflection (Lorentz force) along the Néel walls in contrast to Bloch walls where it is perpendicular. The weak apparent contrast is caused by a small tilt perpendicular to the experimentally adjustable rotation axis (horizontal direction). The existence of magnetic domains/domain walls is proven by tilting the sample by 30° and observing a large contrast change at the domain boundaries (Figure 3g–i). The associated domain pattern agrees well with those visualized with X-ray microscopy (Figure 1c). The domain boundary contrast follows a sinusoidal dependence as a function of the tilt angle (–30° to 30°) according to the projection of the normal magnetization

in domains near the domain wall, and inverts for negative values. Although Néel walls are invisible to Lorentz microscopy, the absence of Bloch lines under normal illumination (Figure 3d,e) serves as an indicator for a chirality selection, i.e., chiral Néel walls.

It turns out that the outlined criteria for chiral ferrimagnetism, i.e., optimal GdCo thickness (≈2 nm) and asymmetric stacking (DMI), are required but insufficient. In fact, a slight increase of the Co content towards a composition of $x = (18 \pm 2)\%$ alters the magnetic domain wall structure in the asymmetric GdCo ($A2_{18}$) stack (Figure 3j,k). A contrast becomes visible at normal incidence, though less pronounced than that of the symmetric (S2) GdCo stack (Figure 3a,b) with the same saturation magnetization (Figure 1b). The latter leads to a similar domain morphology. The emergence of magnetic contrast implies a domain wall with both Bloch and Néel character (Figure 3l), since the increased net saturation magnetization with respect to A2 (Figure 1b) is causing a larger magnetic induction. The hybridization can be assigned to an enlarged magnetostatic energy contribution for Néel walls that is lowered by transformation into Bloch walls. This leads to the intriguing idea that temperature changes may enable tailored domain wall transitions in chiral magnetic systems.

In conclusion, we have presented experimental evidence for chiral ferrimagnetism in soft-magnetic amorphous GdCo multilayer stacks. Our results show a strong dependence of ferrimagnetic properties, such as saturation magnetization, spin and orbital moments, anisotropy, etc., on film thickness, capping and composition. In particular, Co and Gd spin moments are highly susceptible to capping and thickness variations, respectively. We found that a 2 nm thick GdCo film preserves ferrimagnetism with a substantial rare-earth contribution while ensuring a chirality selection through a significant interfacial DMI. Depending on the rare-earth composition either chiral Néel or chiral hybrid Bloch-Néel walls are stabilized in asymmetric GdCo multilayer stacks, which suggest a possible temperature control of domain walls. The domain walls were imaged by high-resolution Lorentz microscopy in combination with exit wave reconstruction that allows for retrieving low and high frequency components of weak magnetic induction (low saturation magnetization). Although the studies were carried out on samples with nonvanishing net magnetization stabilizing magnetic domain walls, the results can be generalized to (nearly) compensated ferrimagnets with electrically excited Skyrmions opening the door to further fundamental investigations and novel applications. The enhanced complexity of chiral amorphous ferrimagnetism compared with its ferromagnetic counterpart calls for future systematic studies facilitating spin DFT[47] and micromagnetics with atomistic resolution.[48] The common approximation of the ferrimagnet as a ferromagnet in micromagnetic simulations is highly inaccurate due to the neglect of underlying mechanisms as confirmed by our experimental work.

Supporting Information

Supporting Information is available from the Wiley Online Library or from the author.

Acknowledgements

This work was primarily funded by the U.S. Department of Energy, Office of Science, Basic Energy Sciences, Materials Sciences and Engineering Division under Contract No. DE-AC02-05-CH11231 within the NEMM program (MSMAG). Work at the Molecular Foundry/National Center for Electron Microscopy was supported by the U.S. Department of Energy, Office of Science, Basic Energy Sciences under Contract No. DE-AC02-05-CH11231. This research used resources of the Advanced Light Source, which is a DOE Office of Science User Facility under contract no. DE-AC02-05CH11231. The authors thank Mi-Young Im for support at the XM-1 beamline at the ALS, and Benjamin McMorran and Antoine Wojdyla for fruitful discussions on wave propagation and exit wave reconstruction.

Conflict of Interest

The authors declare no conflict of interest.

Keywords

chiral domain walls, ferrimagnetism, Lorentz microscopy, thin films, X-ray microspectroscopy

Received: January 9, 2018
Revised: April 10, 2018
Published online: May 23, 2018

[1] I. E. Dzyaloshinskii, *Sov. Phys. JETP* **1957**, *5*, 1259.
[2] T. Moriya, *Phys. Rev.* **1960**, *120*, 91.
[3] A. N. Bogdanov, U. K. Roessler, *Phys. Rev. Lett.* **2001**, *87*, 037203.
[4] R. Wiesendanger, *Nat. Rev.* **2016**, *1*, 16044.
[5] G. Chen, J. Zhu, A. Quesada, J. Li, A. T. N'Diaye, Y. Huo, T. P. Ma, Y. Chen, H. Y. Kwon, C. Won, Z. Q. Qiu, A. K. Schmid, Y. Z. Wu, *Phys. Rev. Lett.* **2013**, *110*, 177204.
[6] G. Chen, T. Ma, A. T. N'Diaye, H. Kwon, C. Won, Y. Wu, A. K. Schmid, *Nat. Commun.* **2013**, *4*, 2671.
[7] W. Jiang, P. Upadhyaya, W. Zhang, G. Yu, M. B. Jungfleisch, F. Y. Fradin, J. E. Pearson, Y. Tserkovnyak, K. L. Wang, O. Heinonen, S. G. E. te Velthuis, A. Hoffmann, *Science* **2015**, *349*, 283.
[8] S. Woo, K. Litzius, B. Kruger, M.-Y. Im, L. Caretta, K. Richter, M. Mann, A. Krone, R. M. Reeve, M. Weigand, P. Agrawal, I. Lemesh, M.-A. Mawass, P. Fischer, M. Klaui, G. S. D. Beach, *Nat. Mater.* **2016**, *15*, 501.
[9] C. Moreau-Luchaire, C. Moutafis, N. Reyren, J. Sampaio, C. A. F. Vaz, N. Van Horne, K. Bouzehouane, K. Garcia, C. Deranlot, P. Warnicke, P. Wohlhu¨ter, J.-M. George, M. Weigand, J. Raabe, V. Cros, A. Fert, *Nat. Nanotechnol.* **2016**, *11*, 444.
[10] F. Hellman, A. Hoffmann, Y. Tserkovnyak, G. S. D. Beach, E. E. Fullerton, C. Leighton, A. H. MacDonald, D. C. Ralph, D. A. Arena, H. A. Duerr, P. Fischer, J. Grollier, J. P. Heremans, T. Jungwirth, A. V. Kimel, B. Koopmans, I. N. Krivorotov, S. J. May, A. K. Petford-Long, J. M. Rondinelli, N. Samarth, I. K. Schuller, A. N. Slavin, M. D. Stiles, O. Tchernyshyov, A. Thiaville, B. L. Zink, *Rev. Mod. Phys.* **2017**, *89*, 025006.
[11] I. M. Miron, T. Moore, H. Szambolics, L. D. Buda-Prejbeanu, S. Auffret, B. Rodmacq, S. Pizzini, J. Vogel, M. Bonfim, A. Schuhl, G. Gaudin, *Nat. Mater.* **2011**, *10*, 419.
[12] A. Manchon, H. C. Koo, J. Nitta, S. M. Frolov, R. A. Duine, *Nat. Mater.* **2015**, *14*, 871.
[13] G. E. W. Bauer, E. Saitoh, B. J. van Wees, *Nat. Mater.* **2012**, *11*, 391.

[14] S. Gepraegs, A. Kehlberger, F. D. Coletta, Z. Qiu, E.-J. Guo, T. Schulz, C. Mix, S. Meyer, A. Kamra, M. Althammer, H. Huebl, G. Jakob, Y. Ohnuma, H. Adachi, J. Barker, S. Maekawa, G. E. W. Bauer, E. Saitoh, R. Gross, S. T. B. Goennenwein, M. Klaui, *Nat. Commun.* **2016**, *7*, 10452.
[15] C. D. Stanciu, F. Hansteen, A. V. Kimel, A. Kirilyuk, A. Tsukamoto, A. Itoh, T. Rasing, *Phys. Rev. Lett.* **2007**, *99*, 047601.
[16] S. Mangin, M. Gottwald, C.-H. Lambert, D. Steil, V. Uhlir, L. Pang, M. Hehn, S. Alebrand, M. Cinchetti, G. Malinowski, Y. Fainman, M. Aeschlimann, E. E. Fullerton, *Nat. Mater.* **2014**, *13*, 286.
[17] M. H. Seaberg, B. Holladay, J. C. T. Lee, M. Sikorski, A. H. Reid, S. A. Montoya, G. L. Dakovski, J. D. Koralek, G. Coslovich, S. Moeller, W. F. Schlotter, R. Streubel, S. D. Kevan, P. Fischer, E. E. Fullerton, J. L. Turner, F.-J. Decker, S. K. Sinha, S. Roy, J. J. Turner, *Phys. Rev. Lett.* **2017**, *119*, 067403.
[18] J. Barker, O. A. Tretiakov, *Phys. Rev. Lett.* **2016**, *116*, 147203.
[19] I. A. Campbell, *J. Phys. F: Metal Phys.* **1972**, *2*, L47.
[20] K. Inoue, K. Kikuchi, M. Ohba, H. Okawa, *Angew. Chem., Int. Ed.* **2003**, *42*, 4810.
[21] S. S. P. Parkin, M. Hayashi, L. Thomas, *Science* **2008**, *320*, 190.
[22] A. Fert, V. Cros, J. Sampaio, *Nat. Nanotechnol.* **2013**, *8*, 152.
[23] M. Finazzi, M. Savoini, A. R. Khorsand, A. Tsukamoto, A. Itoh, L. Duo, A. Kirilyuk, T. Rasing, M. Ezawa, *Phys. Rev. Lett.* **2013**, *110*, 177205.
[24] Y. Mimura, N. Imamura, T. Kobayashi, A. Okada, Y. Kushiro, *J. Appl. Phys.* **1978**, *49*, 1208.
[25] P. Hansen, C. Clausen, G. Much, M. Rosenkranz, K. Witter, *J. Appl. Phys.* **1989**, *66*, 756.
[26] R. J. Gambino, J. J. Cuomo, *J. Vac. Sci. Technol.* **1978**, *15*, 296.
[27] F. Hellman, E. M. Gyorgy, *Phys. Rev. Lett.* **1992**, *68*, 1391.
[28] V. G. Harris, K. D. Aylesworth, B. N. Das, W. T. Elam, N. C. Koon, *Phys. Rev. Lett.* **1992**, *69*, 1939.
[29] Y. Mimura, N. Imamura, T. Kobayashi, *IEEE Trans. Magn.* **1976**, *12*, 779.
[30] M. S. El Hadri, M. Hehn, P. Pirro, C.-H. Lambert, G. Malinowski, E. E. Fullerton, S. Mangin, *Phys. Rev. B* **2016**, *94*, 064419.
[31] B. Hebler, A. Hassdenteufel, P. Reinhardt, H. Karl, M. Albrecht, *Front. Mater.* **2016**, *3*, 8.
[32] J. J. Chess, S. A. Montoya, E. E. Fullerton, B. J. McMorran, *AIP Adv.* **2017**, *7*, 056807.
[33] D. Paganin, K. A. Nugent, *Phys. Rev. Lett.* **1998**, *80*, 2586.
[34] M. De Graef, Y. Zhu, *J. Appl. Phys.* **2001**, *89*, 7177.
[35] C. Phatak, A. K. Petford-Long, M. De Graef, *Phys. Rev. Lett.* **2010**, *104*, 253901.
[36] T. Tanigaki, Y. Takahashi, T. Shimakura, T. Akashi, R. Tsuneta, A. Sugawara, D. Shindo, *Nano Lett.* **2015**, *15*, 1309.
[37] R. Streubel, F. Kronast, P. Fischer, D. Parkinson, O. G. Schmidt, D. Makarov, *Nat. Commun.* **2015**, *6*, 7612.
[38] C. Donnelly, M. Guizar-Sicairos, V. Scagnoli, S. Gliga, M. Holler, J. Raabe, L. J. Heyderman, *Nature* **2017**, *547*, 328.
[39] H. Yang, A. Thiaville, S. Rohart, A. Fert, M. Chshiev, *Phys. Rev. Lett.* **2015**, *115*, 267210.
[40] J. Geissler, E. Goering, M. Justen, F. Weigand, G. Schuetz, J. Langer, D. Schmitz, H. Maletta, R. Mattheis, *Phys. Rev. B* **2001**, *65*, 020405.
[41] B. T. Thole, P. Carra, F. Sette, G. van der Laan, *Phys. Rev. Lett.* **1992**, *68*, 1943.
[42] P. Carra, B. T. Thole, M. Altarelli, X. Wang, *Phys. Rev. Lett.* **1993**, *70*, 694.
[43] R. Wu, A. J. Freeman, *Phys. Rev. Lett.* **1994**, *73*, 1994.
[44] C. T. Chen, Y. U. Idzerda, H.-J. Lin, N. V. Smith, G. Meigs, E. Chaban, G. H. Ho, E. Pellegrin, F. Sette, *Phys. Rev. Lett.* **1995**, *75*, 152.
[45] Y. Teramura, A. Tanaka, B. Thole, T. Jo, *J. Phys. Soc. Jpn.* **1996**, *65*, 3056.
[46] R. W. Gerchberg, W. O. Saxton, *Optik* **1972**, *35*, 227.
[47] C. R. Jacob, M. Reiher, *Int. J. Quantum Chem.* **2012**, *112*, 3661.
[48] C. Andreas, A. Kakay, R. Hertel, *Phys. Rev. B* **2014**, *89*, 134403.

